

Accepted for publication in *Astrophysical Journal* April 27, 2000

EUVE Observations of OY Carinae in Superoutburst

Christopher W. Mauche

*Lawrence Livermore National Laboratory,
L-43, 7000 East Avenue, Livermore, CA 94550;
mauche@cygnus.llnl.gov*

and

John C. Raymond

*Harvard-Smithsonian Center for Astrophysics,
60 Garden Street, Cambridge, MA 02138;
jraymond@cfa.harvard.edu*

ABSTRACT

The *Extreme Ultraviolet Explorer* (*EUVE*) satellite was used for three days beginning on 1997 Mar 26.96 UT to obtain photometric and spectroscopic observations of the eclipsing SU UMa-type dwarf nova OY Carinae in superoutburst. Because of the longer time on source (143 ks), the larger number of eclipses observed (17), and the higher count rate in the detector (0.5–2.2 counts s^{−1}), we are able to significantly strengthen previous reports that there is little or no eclipse by the secondary of the EUV emission region of OY Car in superoutburst. The mean *EUVE* spectrum extends from 70 to 190 Å and contains broad (FWHM ≈ 1 Å) emission lines of N V, O V–O VI, Ne V–Ne VII, Mg IV–Mg VI, Fe VI–Fe VIII, and possibly Fe XXIII. Good fits of the observed spectrum are obtained with a model (similar to that of Seyfert 2 galaxies) wherein radiation from the boundary layer and accretion disk is scattered into the line of sight by the system’s photoionized accretion disk wind. It is possible to trade off continuum luminosity for wind optical depth, but reasonable models have a boundary layer temperature $T_{\text{bl}} \approx 90\text{--}130$ kK and a boundary layer and accretion disk luminosity $L_{\text{bl}} = L_{\text{disk}} \lesssim 4 \times 10^{34}$ erg s^{−1} ≈ 10 L_⊙, corresponding to a mass-accretion rate $\dot{M}_{\text{a}} \lesssim 10^{-8}$ M_⊙ yr^{−1}; an absorbing column density $N_{\text{H}} \approx 1.6\text{--}3.5 \times 10^{19}$ cm^{−2}; and a wind mass-loss rate $\dot{M}_{\text{w}} \lesssim 10^{-10}$ M_⊙ yr^{−1} ≈ 0.01 \dot{M}_{a} . Because radiation pressure alone falls an order of magnitude short of driving such a wind, magnetic forces must also play a role in driving the wind of OY Car in superoutburst.

Subject headings: binaries: close — binaries: eclipsing — novae, cataclysmic variables — stars: individual (OY Carinae) — stars: winds, outflows — ultraviolet: stars

1. Introduction

Cataclysmic variables (CVs) are a diverse class of semidetached binaries composed typically of a low-mass main-sequence secondary, an accreting white dwarf, and a luminous accretion disk. There are three generalized classes of CVs: novae, novalike variables, and dwarf novae. In dwarf novae, a mass-transfer instability causes the disk to brighten by 3–5 magnitudes in the optical at quasi-periodic intervals of tens to hundreds of days. Based on their light curve morphologies, most dwarf novae are classified as either U Gem systems with “normal” outbursts only, Z Cam systems with “normal” outbursts and prolonged states of intermediate brightness (“standstills”), or SU UMa systems with “normal” and “super” (brighter, longer-duration) outbursts. Nonmagnetic novalike variables behave like dwarf novae “stuck” in outburst. Warner (1995) provides an excellent background on all of the various CV types and subtypes, while Cannizzo (1993) and Osaki (1996) provide recent reviews of the theory of dwarf nova outbursts.

While the white dwarf and accretion disk are the dominant sources of optical through FUV light in dwarf novae, the boundary layer between the disk and the surface of the white dwarf is the dominant source of higher-energy emission. Modulo a correction factor for white dwarf rotation, the boundary layer luminosity $L_{\text{bl}} = GM_{\text{wd}}\dot{M}_{\text{a}}/2R_{\text{wd}} \sim 4 \times 10^{34} (\dot{M}_{\text{a}}/10^{-8} \text{ M}_{\odot} \text{ yr}^{-1}) \text{ erg s}^{-1}$, where \dot{M}_{a} is the accretion rate and M_{wd} and R_{wd} are respectively the mass and radius of the white dwarf. When \dot{M}_{a} is low (e.g., dwarf novae in quiescence), the boundary layer is optically thin and quite hot (of order the virial temperature $T_{\text{vir}} = GM_{\text{wd}}m_{\text{H}}/3kR_{\text{wd}} \sim \text{tens of keV}$; Pringle & Savonije 1979; Tylenda 1981; Narayan & Popham 1993); when \dot{M}_{a} is high (e.g., novalike variables and dwarf novae in outburst), the boundary layer is optically thick and quite cool (of order the blackbody temperature $T_{\text{bb}} = [GM_{\text{wd}}\dot{M}_{\text{a}}/8\pi\sigma R_{\text{wd}}^3]^{1/4} \sim 100 \text{ kK}$; Pringle 1977; Tylenda 1977; Popham & Narayan 1995).

Observationally, the location and extent of the source of the X-rays in nonmagnetic CVs is constrained by (1) the X-ray light curves of eclipsing systems, (2) the variation of apparent emission measure with binary inclination (van Teeseling, Beuermann, & Verbunt 1996), and (3) the relative strength of the line and continuum spectrum reflected off the white dwarf and accretion disk (e.g., Done & Osborne 1997). All these constraints imply that all or most of the hard X-rays in low- \dot{M} CVs are emitted very close to the white dwarf, but the eclipse observations provide the most direct and unambiguous evidence. In HT Cas ($i \approx 81^\circ$; Wood et al. 1995; Mukai et al. 1997), Z Cha ($i \approx 82^\circ$; van Teeseling 1997), and OY Car ($i \approx 83^\circ$; Pratt et al. 1999a) in quiescence, the X-rays are fully eclipsed for an orbital phase interval comparable to that of the optical eclipse of the white dwarf.

In contrast to the compact source of hard X-rays in low- \dot{M} CVs, there is strong evidence for an extended source of soft X-rays in high- \dot{M} CVs. *EXOSAT* and *ROSAT* light curves of OY Car in superoutburst (Naylor et al. 1988; Pratt et al. 1999b) and *ROSAT* light curves of the novalike variable UX UMa ($i \approx 71^\circ$; Wood, Naylor, & Marsh 1995) rule out an eclipse by the secondary of a compact source of X-rays centered on the white dwarf. In both cases, it is argued that the

boundary layer is obscured from view by the accretion disk at all orbital phases, and that the observed X-rays come from a corona or wind above the disk.

The situation is far more complex in U Gem ($i \approx 70^\circ$). In quiescence, the hard X-rays are partially eclipsed at orbital phase $\phi \sim 0.7$ (Szkody et al. 1996), and during outburst the EUV and soft X-rays are partially eclipsed at orbital phases $\phi \sim 0.7$ and 0.1 (Mason et al. 1988; Long et al. 1996). These dips in the X-ray and EUV light curves are interpreted as partial eclipses of the boundary layer by vertical structure at the edge of the accretion disk ($r \approx 4 \times 10^{10}$ cm) or at the circularization radius of the accretion stream ($r \approx 5 \times 10^9$ cm); in either case, the heights above the orbital plane are distressingly large: $h \approx 0.5r$, whereas the disk thickness $H \approx c_s/\Omega_K \ll r$. The *EUVE* spectra of U Gem in outburst supply additional diagnostic information. The phase-averaged spectrum contains emission lines of Ne VI–VIII, Mg VI–VII, and Fe VII–X superposed on a $T = 110\text{--}140$ kK blackbody continuum (Long et al. 1996). The phase-resolved spectra demonstrate that the eclipses affect the continuum more strongly than the lines (most strikingly, the Ne VIII $\lambda 88.1$ line is nearly unaffected by the eclipses; see Mauche 1997), implying that the lines are produced in a region of larger extent than that of the continuum, which presumably is formed in the boundary layer.

To gain a better understanding of the extended source of soft X-rays in high- \dot{M} CVs, we obtained *EUVE* observations of the eclipsing SU UMa-type dwarf nova OY Car in superoutburst. The resulting data are superior to those from the previous *EXOSAT* and *ROSAT* observations because of the longer time on source, the larger number of eclipses observed, the higher count rate in the detector, and the ability to obtain dispersed EUV spectra. We discuss the *EUVE* observations in §2, the DS light curve in §3, and the SW spectrum in §4. We find that there is little or no eclipse of the EUV emission region in OY Car in superoutburst (§3), and that the EUV spectrum contains emission lines of intermediate ionization stages of N, O, Ne, Mg, and Fe (§4). The spectrum is not fit well in detail by a model of a collisionally ionized plasma (§5), and although it is fit well by a model wherein radiation from the boundary layer and accretion disk is scattered into the line of sight by OY Car’s accretion disk wind (§6), radiation pressure alone falls an order of magnitude short of driving the wind (§7). We close in §8 with a discussion and summary of our results.

2. *EUVE* Observations

The events leading up to the *EUVE* observations of OY Car are as follows. On 1997 Mar 25.46 UT M. Mattiazzo posted an alert to VSNET (#802) and the AAVSO that OY Car had gone into outburst. On Mar 25.76 this alert was transmitted to us by J. Mattei, Director of the AAVSO. Less than an hour after being contacted by us (and despite the fact that the *EUVE* Peer Review was ongoing), *EUVE* Acting Deputy Director J. Vallergera granted our request for target-of-opportunity observations of OY Car. On Mar 26.13 M. Keane, responding to a request posted by us to VSNET (#804), provided independent confirmation of the outburst in the form of an image of the OY Car

field obtained by N. Suntzeff with the 0.9-m telescope at CTIO. In the hours leading up to the start of *EUVE* observations on Mar 26.96, photometric estimates were provided by M. Mattiazzo, P. Nelson, R. Stubbings, T. Cragg, and J. Herr.

The optical light curve of the 1997 March/April outburst of OY Car, assembled from observations submitted to and obtained from the AAVSO (J. A. Mattei 1997, personal communication) and VSS/RASNZ (F. M. Bateson 1997, personal communication) is shown in Figure 1. Based on its peak brightness ($V \approx 11$) and duration ($\Delta t \approx 20$ days), this event was clearly a superoutburst. According to the records of the AAVSO, the previous and subsequent two outbursts of OY Car took place in 1995 October/November (a superoutburst), 1997 July/August (a normal outburst), and 1998 February (a superoutburst). For Figure 1, we have suppressed observations obtained near, and hence affected by, the eclipse by the secondary of the white dwarf and accretion disk. Specifically, we assume the binary ephemeris of Pratt et al. (1999a) and retain only those observations for which the binary phase was in the range $\phi = 0.1$ – 0.9 . The amplitude of the scatter remaining in the light curve is reasonably consistent with that expected for AAVSO and RASNZ data for such a relatively dim source.

EUVE observations of OY Car began on 1997 Mar 26.96 UT, ran for three days ($\text{JD} - 2450000 = 534.457$ – 537.636), and resulted in a total of 143 ks of exposure. For a description of the *EUVE* satellite and instrumentation, refer to Bowyer & Malina (1991), Abbott et al. (1996), and Sirk et al. (1997). It is sufficient to note here that the bandpasses of the deep survey (DS) photometer and short wavelength (SW) spectrometer are defined by a Lexan/Boron filter and extend from ≈ 70 to ≈ 180 Å. The medium wavelength (MW) spectrometer bandpass is defined by an Aluminum/Carbon filter and extends from ≈ 170 to ≈ 370 Å, but interstellar absorption extinguishes the flux longward of about 200 Å. These observations were “spiral dithered” to avoid the dead spot near the center of the field of view of the DS instrument, and to increase the signal-to-noise ratio of the EUV spectrum by averaging over quantum efficiency variations of the SW detector.

3. DS Light Curve

The background-subtracted DS count rate light curve from our observations is shown in Figure 2 and in Figure 1 superposed on the optical light curve. The data are binned into detector “good time intervals” of typically ≈ 1950 s, so the error bars are typically smaller than the points. Given that the optical light curve was constant or declining only gradually during the *EUVE* observation, the relatively rapid decline and subsequent rise of the DS light curve is something of a surprise. The observation is unfortunately too short to know for sure, but the similarity to the *Voyager* FUV light curve of VW Hyi in superoutburst (Polidan & Holberg 1987; Pringle et al. 1987) suggests that we are seeing in the EUV the decay of a narrow outburst and the subsequent rise of a long outburst which “add” to produce the superoutburst. This behavior is at least in qualitative agreement with the thermal-tidal instability model of superoutbursts (Osaki 1996): a normal outburst is triggered by the disk thermal instability (Cannizzo 1993), which in turn triggers the tidal instability when the disk expands out to the 3:1 eccentric inner Lindblad resonance (Lubow 1991); the resulting

enhanced tidal torques enhance the mass-accretion rate through the disk, rejuvenating the initial outburst. Credence for this interpretation is supplied by the SPH simulations of Murray (1998, Fig. 11), but better (more extensive, multiwavelength) data are required to convincingly test this interpretation.

One of the purposes of the *EUVE* observation of OY Car was a study of the eclipses (or lack thereof) of the EUV emission region by the secondary, but this is made difficult by the strong commensurability between *EUVE*’s orbital period (94.6 min) and OY Car’s binary period (90.9 min). The result is that the binary phase advances by only 4% each satellite orbit, and eclipse intervals “come around” only every 1.6 days. The net result is that during three days of observations we recorded only 17 eclipses of the white dwarf. The orbits during which these eclipses occurred are indicated by the circles in Figure 2. During two of these orbits we are both fortunate and lucky to have a detailed record of the optical behavior of the source measured by W. S. G. Walker (1997, personal communication) with a 10-in telescope and a ST6 CCD camera. The EUV and optical light curves during the interval of optical measurements are shown in Figure 3, where the phase is relative to the binary ephemeris of Pratt et al. (1999a) and the grey stripes denote the intervals when the white dwarf is eclipsed by the secondary ($-0.02 \leq \phi \leq +0.02$). Whereas the optical light curve clearly shows the prominent eclipses of the accretion disk by the secondary, there is no hint of eclipses in the EUV light curve.

To help quantify this statement, we determined the DS count rate light curves for each of the intervals containing an eclipse of the white dwarf. These are shown in the upper panel of Figure 4. To increase the photon statistics and decrease the effect of the flickering apparent in the DS light curves, we calculated the mean DS count rate light curves for the two groups of eight intervals of white dwarf eclipses. Exactly how this is done is somewhat subjective, but proper account has to be made of the different count rates during each interval i and the different exposure times within each phase bin j . The former was accounted for by fitting the background-subtracted DS count rate data with a linear function $f_{ij} = a_i + b_i(\phi_j - \phi_{0,i})$, where $\phi_{0,i}$ is the midpoint of interval i . If S_{ij} and B_{ij} are the counts from the source and background regions, respectively, and Δt_{ij} are the deadtime and primsch-corrected exposure times, the mean relative DS count rate light curves are $(\sum_i S_{ij} - 0.2 \sum_i B_{ij}) / (\sum_i \Delta t_{ij} \sum_i f_{ij})$, where the factor of 0.2 accounts for the relative size of the source and background regions. The resulting two mean relative DS count rate light curves are shown in the lower panels of Figure 4, where we have retained only those phase bins sampled at least five times during the eight intervals of white dwarf eclipses. What one concludes about the depth of the eclipse of the EUV emission region depends sensitively on the assumed width of the eclipse and the assumed shape of the uneclipsed light curve. During the first interval the DS light curve is well behaved and a secure upper limit is 5% at the 90% confidence level. During the second interval the DS light curve is less well behaved, but a reasonable upper limit is 15% at the 90% confidence level. These results significantly strengthen the conclusion based on previous *EXOSAT* (Naylor et al. 1988) and *ROSAT* (Pratt et al. 1999b) observations that there is little or no eclipse by the secondary of the EUV emission region of OY Car in superoutburst.

4. SW Light Curve and Spectrum

The SW spectrometer provides an independent measurement of the EUV light curve of OY Car, but it is less useful than the DS photometer to study the eclipses because it has approximately one-tenth the effective area and (because the flux is dispersed over many more detector pixels) a higher effective background. The upper panel of Figure 5 shows the background-subtracted SW count rate between 90 and 180 Å, while the lower panel shows the SW hardness ratio, defined as the ratio of the background-subtracted SW counts from 90–125 Å to that from 125–180 Å. As in Figure 2, the data are binned into detector “good time intervals” of typically ≈ 1950 s, and the intervals during which eclipses occurred are indicated by the circles. The upper panel demonstrates that the SW light curve is reasonably consistent with the DS light curve within the errors, while the lower panel reveals a mild spectral evolution during the observation. A constant $r = a$ fit to the hardness ratio produces $\chi^2/\text{dof} = 72.8/49 = 1.49$ with $a = 0.77 \pm 0.03$, a linear fit $r = a + bt$ produces $\chi^2/\text{dof} = 51.5/48 = 1.07$ with $b = -0.12 \pm 0.03$, and a quadratic fit $r = a + bt + ct^2$ produces $\chi^2/\text{dof} = 42.7/47 = 0.91$ with $c = -0.10 \pm 0.03$. As measured by the F test, each additional degree of freedom decreases χ^2 sufficiently to require the additional parameter with $> 99\%$ confidence. This establishes a real but weak correlation of the hardness ratio with the SW count rate.

To investigate this spectral evolution further, we constructed a pseudotrained SW spectrum of OY Car by concatenating individual spectra accumulated during the various SW “good time intervals.” The result is shown in Figure 6, where the upper panel shows the spectra as observed, and the lower panel shows the spectra with the count rate evolution removed (with the individual spectra normalized to an equal number of counts between 90 and 180 Å). With the count rate evolution removed, the spectrum is seen to be quite stable throughout the observation: there are strong emission lines at $\approx 114, 123, 131, 136, 138, 144, 150$, and 168 Å, plus what appears to be a weak continuum which peaks at ~ 120 Å. The only obvious spectral variations are in the relative normalization of the lines and continuum—the lines being relatively stronger toward the middle of the observation, and the continuum being relatively stronger at beginning and end of the observation. These variations are sufficiently subtle to allow us to assemble a mean spectrum of OY Car from the entire observation.

To accomplish this, we maximized the signal-to-noise ratio by combining data from the SW spectrometer from 90 to 175 Å and data from the MW spectrometer from 170 to 190 Å; the overlap from 170 to 175 Å lends confidence in the emission feature at ≈ 172 Å. The resulting mean *EUVE* spectrum of OY Car is shown in Figure 7, where the SW spectrum is binned to 0.25 Å, the MW spectrum is binned to 0.5 Å (roughly half the FWHM of the spectral resolution of the two spectrometers), and the traces at the bottom of the figure show the associated 1σ error vectors. If it is not immediately obvious, a look through the *EUVE* Stellar Spectral Atlas (Craig et al. 1997) will convince the reader that the mean *EUVE* spectrum of OY Car is like that of no other class of objects: it lacks the strong continuum of hot white dwarfs, it lacks the narrow high-excitation emission lines of late-type stars and RS CVn binaries, it doesn’t look like the spectra of polars, intermediate polars, or even other dwarf novae. Instead, the spectrum is dominated by broad

(FWHM ≈ 1 Å) emission lines, and the continuum is weak and can be plausibly described as a superposition of numerous weak emission lines.

In an attempt to quantitatively determine the parameters (wavelength, width, and flux) of the various emission features, we fit the mean SW spectrum of OY Car from 94.5 to 173.5 Å with a number of Gaussians. Of order 40 Gaussians were required to “iron out” the residuals, but with 316 data points and of order 120 free parameters, the fits tended to be unstable (minor variations in the initial parameters resulted in major variations in the fit parameters). Instead, reasonable and stable fits were obtained with 44 Gaussians with prescribed widths. In one fit, the Gaussian widths σ were fixed at a common value, while in another they varied with the central wavelength of the Gaussians as $\sigma_i = [0.212^2 + (\lambda_i \Delta v / c)^2]^{1/2}$. The latter choice reproduces the FWHM of the SW spectrometer if $\Delta v = 0$ and accounts for the broadening of the lines by Doppler processes. The best fits were obtained with either $\sigma = 0.46$ Å (hence the intrinsic FWHM = 0.96 Å) or $\Delta v = 975$ km s $^{-1}$ (hence the intrinsic FWHM = 2300 km s $^{-1}$). The parameters from the latter more physical fit are listed in Table 1.

By comparing the data in Table 1 to the Kelly (1987); Mewe, Gronenschild, & van den Oord (1985); and Verner, Verner, & Ferland (1996) line lists, one sees that a consistent interpretation of the EUV spectrum of OY Car can be had with lines from intermediate ionization stages of cosmically abundant N, O, Ne, Mg, and Fe. The five brightest lines are identified as follows: 122.9 Å: Ne VI $2p-3d$, 143.5 Å: Ne V $2p^2-2p3d$, 168.5 Å: Fe VIII $3p^63d-3p^53d^2$, 131.3 Å: Fe VIII $3d-4f$, and 150.3 Å: O VI $2s-3p$. These identifications alone significantly constrain the physical nature of the emitting plasma. If collisionally ionized, its temperature must lie in the range $\log T(\text{K}) \approx 5.4-5.6$. If photoionized, its ionization parameter $\xi \equiv L/nr^2$ must lie in the range $\log \xi \approx 0-5$. Because all of the above strong lines are resonance lines, scattering in a photoionized plasma is the more likely mechanism responsible for the observed spectrum, but a detailed investigation, provided in the next two sections, is required to defend this statement.

5. Spectrum of a Collisionally Ionized Plasma

To construct a model spectrum of a collisionally ionized plasma, we used the suite of IDL programs distributed with version 2 of the CHIANTI atomic database (Landi et al. 1999). We assumed the elemental abundances of Allen (1973); the ionization equilibrium curves of Mazzotta et al. (1998); an absorbing column density $N_{\text{H}} = 1-10 \times 10^{19}$ cm $^{-2}$; a distance $d = 85$ pc, consistent with the values derived by Wood et al. (1989) and Bruch et al. (1996); and a temperature $T = 10^5-10^6$ K, incremented in steps of 0.1 in the log. As shown in Figure 8, a model with $\log T(\text{K}) = 5.5$, $N_{\text{H}} = 3.4 \times 10^{19}$ cm $^{-2}$, and an emission measure $EM \equiv \int n_e^2 dV = 3.2 \times 10^{55}$ cm $^{-3}$ does a reasonable job of reproducing the strongest lines of O VI, Ne V, and Ne VI. The strength of the Fe VIII $\lambda 131.1$ emission line can be reproduced if the ionization fraction χ of Fe VIII is increased by a factor of approximately two from its value of $\chi = 0.4$ at $\log T(\text{K}) = 5.5$, but none of Arnaud & Rothenflug (1985), Arnaud & Raymond (1992), or Mazzotta et al. (1998) have Fe VIII peaking above $\chi = 0.5$,

implying that the Fe abundance must be enhanced by a similar factor to reproduce the data. The Fe VIII $\lambda 168.6$ emission line is not reproduced by the model because the data for that transition is missing from the CHIANTI database. Similarly, the model is incapable of reproducing the O V $\lambda\lambda 139.0, 135.5, 124.6$, or 118.0 emission features because the database is missing lines of O V shortward of 166 \AA . A more severe problem is the spectrum of O VI, which is shown shaded in Figure 8: many of the predicted lines are too strong relative to the data. Particularly egregious are the $\lambda 115.8$ $2s\text{--}4p$ resonance line and the $\lambda 129.8$ $2p\text{--}4d$ and $\lambda 173.0$ $2p\text{--}3d$ nonresonance lines. The $\lambda 173$ line can be reduced in strength by increasing the absorbing column density, but this makes the problem with the $\lambda 130$ line worse. Both the $\lambda 173/\lambda 150$ and $\lambda 130/\lambda 150$ line ratios can be decreased by increasing the density, but values in excess of 10^{14} cm^{-3} are required. Finally, optical depth effects would be expected to *decrease* the strength of the resonances lines, hence to *increase* the $\lambda 173/\lambda 150$ and $\lambda 130/\lambda 150$ line ratios, making the problem worse. Given these problems, it seems unlikely that the EUV spectrum of OY Car is produced by a collisionally ionized plasma.

6. Spectrum of Scattering in a Photoionized Plasma

To produce a scattering model of the EUV spectrum of OY Car, we need to specify the EUV spectral energy distribution F_λ ; the wind geometry, velocity law $v(r)$, and mass-loss rate \dot{M}_w ; the absorbing column density N_H ; the source distance d ; and the relevant atomic data. Specifically, in the Sobolev approximation, the scattered intensity is $F_\lambda (1 - e^{-\tau_\lambda})$, where the optical depth $\tau_\lambda = (\pi e^2 / m_e c) n A \chi \lambda_{ij} f_{ij} (g_i / \Sigma g_i) (dv/dr)^{-1}$, n is the density, A are the abundances, χ are the ionization fractions, dv/dr is the wind velocity gradient, and λ_{ij} , f_{ij} , and g_i are respectively the wavelengths, oscillator strengths, and statistical weights of the various transitions. We assume that the abundances are as given by Allen (1973), the atomic data are as given by Verner, Verner, & Ferland (1996), and the EUV spectral energy distribution is dominated by that of the boundary layer, which radiates like a blackbody with temperature T_{bl} and luminosity $L_{bl} = 4\pi R_{wd}^2 f \sigma T_{bl}^4 = 4.3 \times 10^{34} f (T_{bl}/10^5 \text{ K})^4 \text{ erg s}^{-1}$, where $R_{wd} = 7.8 \times 10^8 \text{ cm}$ is the radius appropriate to a $0.7 M_\odot$ white dwarf and f is the fractional emitting area of the boundary layer.

The observed spectrum can be used to constrain the possible values of T_{bl} , N_H , and f : if the boundary layer temperature is too high there is too much flux at the shortest wavelengths; if the absorbing column density is too low there is too much flux at the longest wavelengths; if the area of the boundary layer is too small it will not produce the observed flux. These constraints are shown in the upper panel of Figure 9, where we plot as a function of T_{bl} and N_H the value of f required to reproduce the observed flux density. Consider the shape of the $f = 1$ curve, for which the absorbed blackbody flux distribution “drapes” over the emission lines of the observed spectrum. At low temperatures and absorbing column densities the constraint is set by the peak flux density of the 96 \AA emission line; as the temperature increases the constraint switches to the 123 \AA emission line; at even higher temperatures the constraint switches to the 168 \AA emission line. The dotted curves in Figure 9 show where these transitions take place. Favorable models

simultaneously satisfy the 123 and 168 Å constraints, so lie near the upper dotted curve: $T_{\text{bl}} = 80\text{--}140$ kK, $N_{\text{H}} \approx 1.6\text{--}4 \times 10^{19} \text{ cm}^{-2}$, and $f \approx 0.01\text{--}20$, hence $L_{\text{bl}} \approx 2\text{--}350 \times 10^{33} \text{ erg s}^{-1}$. Models in the upper hatched region of the figure are excluded because they exceed the Eddington limit of a $0.7 M_{\odot}$ white dwarf.

The next step is to specify the parameters of the wind. Rather than attempt a full three-dimensional model, we settle here for a one-zone model and take fiducial values of the relevant parameters: specifically, the velocity gradient $dv/dr = 3000 \text{ km s}^{-1}/10^{10} \text{ cm} = 0.03 \text{ s}^{-1}$ and the density $n = 10^{10} \text{ cm}^{-3}$ at a distance $r = 10^{10} \text{ cm}$; the wind mass-loss rate is then $\dot{M}_{\text{w}} = 4\pi r^2 \mu m_{\text{H}} n v = 1.3 \times 10^{-10} M_{\odot} \text{ yr}^{-1}$. To match the observed widths of the emission lines, the opacity is distributed as a Gaussian with FWHM = 0.96 Å and the resulting model is convolved with a FWHM = 0.5 Å Gaussian to account for the spectral resolution of the SW spectrograph.

To construct a model spectrum within this framework, it is necessary to specify the shape and intensity of the underlying continuum through the parameters T_{bl} , N_{H} , and f , and the optical depths of the lines through the product $nA\chi(dv/dr)^{-1}$. Assuming that n and $(dv/dr)^{-1}$ are as given above, this leaves the three continuum parameters and the set of products $\chi' \equiv A\chi$ to specify a given model. This set of models can be constrained further by considering only the spectrum of Fe VIII, which has strong and reasonably unblended emission lines at 108, 131, 169, and 185 Å. Unfortunately, it proves impossible to reproduce the flux in all four of these emission lines simultaneously, but it is possible to satisfy the constraints imposed by any combination of three. The locus of points for Model Sequence 1 satisfying the 108, 131, 169 Å emission line fluxes is shown in the upper and lower panels of Figure 9 by the lower of the two bold solid curves, while that for Model Sequence 2 satisfying the 108, 131, 185 Å emission line fluxes is shown by the upper of the two curves. In each case the optical depth in the Fe VIII lines is varied by varying $\chi'(\text{Fe VIII}) = [0.01, 0.1, 0.3, 0.6, 1, 2, 3, 6, 10]$ [$\chi'(\text{Fe VIII}) > 1$ if the Fe abundance is greater than solar or if the wind density or velocity gradient are greater than their fiducial values]. At low optical depths and high temperatures Sequence 1 converges on $T_{\text{bl}} = 127$ kK and $N_{\text{H}} = 1.6 \times 10^{19} \text{ cm}^{-2}$, while Sequence 2 converges on $T_{\text{bl}} = 104$ kK and $N_{\text{H}} = 3.1 \times 10^{19} \text{ cm}^{-2}$. The trajectory of both sequences is truncated at high optical depths and low temperatures where the models first fail to provide enough flux to explain the observed strengths of other emission lines (the 123 Å emission line for Sequence 1, the 169 Å emission line for Sequence 2); this happens at $T_{\text{bl}} \approx 100$ kK and $N_{\text{H}} \approx 2.3 \times 10^{19} \text{ cm}^{-2}$ for Sequence 1, and at $T_{\text{bl}} \approx 90$ kK and $N_{\text{H}} \approx 3.5 \times 10^{19} \text{ cm}^{-2}$ for Sequence 2.

From among the above model sequences satisfying the Fe VIII line ratios, we present results for five models. Model 1-7a assumes $T_{\text{bl}} = 107$ kK, $N_{\text{H}} = 2.1 \times 10^{19} \text{ cm}^{-2}$, $f = 0.27$, and $\chi'(\text{Fe VIII}) = 3$; all other ionization fractions are set to one. The resulting model spectrum is shown superposed on the data in the upper panel of Figure 10. By construction, the model matches the flux in the Fe VIII 108, 131, and 169 Å emission lines, but it overpredicts or underpredicts the flux in other lines. Many of these deficiencies can be remedied by adjusting the ionization fractions of the various ions, although blending renders the choices somewhat arbitrary. Careful examination of the models reveals that the strongest emission lines are due to Ne, Fe, and O, but lines from Mg, N, Al, Na,

and Ar (in decreasing order of importance) also contribute; the only lines from Si are from Si V, and the strongest of its two lines lies at 96.4 Å in a gap between two observed lines. Given these results, we set the concentrations of ions of N, Na, Mg, Al, and Ar to 1 and Si to 0. To minimize the flux of lines at and below 172 Å, we set the concentrations of O IV, Ne IV, and Fe IX–Fe XI to 0. The concentrations of the other ions were adjusted to match the observed emission line strengths (specifically, the strength of the lines marked with asterisks in Fig. 10 were adjusted; the strength of the remaining lines follow according to the strength of the local continuum and their optical depths). Table 2 lists the resulting model parameters of this Model 1-7b and the middle panel of Figure 10 shows the resulting model spectrum. The overall match to the data is reasonably good, although the flux in the O V λ 172 and Fe VIII λ 185 emission lines are overpredicted and there are a few lines (e.g., at 128 and 155 Å) which these models are simply incapable of producing. Similar results are obtained for Model 1-5b, for which $\chi'(\text{Fe VIII}) = 1$, so it is not shown in Figure 10. The problem with the Fe VIII λ 185 emission line can be fixed by switching to the Model Sequence 2. The parameters of Model 2-5b [with $\chi'(\text{Fe VIII}) = 1$] and Model 2-3b [with $\chi'(\text{Fe VIII}) = 0.3$] are listed in Table 2 and the Model 2-5b spectrum is shown superposed on the data in the lower panel of Figure 10. These models match the flux in the Fe VIII λ 185 emission line, but underpredict the flux in the Fe VIII λ 169 line. Both model sequences overpredict the flux in the O V λ 172 emission feature, whose strength is determined by the pair of O V emission features at 136 and 139 Å.

These results demonstrate that it is possible to reproduce the essential features of the EUV spectrum of OY Car with a simple model wherein radiation from the boundary layer is scattered into the line of sight by the system’s accretion disk wind. Given the success of this model, we supply in Table 1 likely identifications (ions, transitions, wavelengths, and oscillator strengths) of the observed lines from the Verner, Verner, & Ferland (1996) list of atomic data for permitted resonance lines. Table 1 and Figure 10 show that the important ions in these models are N V, O V–O VI, Ne V–Ne VII, Mg IV–Mg VI, Fe VI–Fe VIII, and Fe XXIII. With the exception of the last ion, the ionization potentials of these species lie between 100 and 200 eV. The 1950 eV ionization potential of Fe XXIII renders the identification of the 133 Å emission feature suspect, but such a high-excitation [$\log T(\text{K}) \approx 7.3$ in collisional ionization equilibrium] component of the wind cannot be excluded by the spectrum, because the Fe XVIII–Fe XXII lines in the SW bandpass are predicted to be weak.

7. Evaluation of the Radiation Force

Although it has been known for over two decades that high- \dot{M} CVs have strong winds (Heap et al. 1978; Krautter 1981; Klare 1982), it is still uncertain what drives the wind. Radiation pressure in spectral lines is implicated by the similarity of the effective temperatures and P Cygni profiles of high- \dot{M} CVs with those of early-type stars, but centripetal acceleration may play a role if the disk is threaded by a large-scale magnetic field (Blandford & Payne 1982; Cannizzo & Pudritz 1988). A minimum requirement of any successful model is that it reproduce the observed wind mass-loss

rates \dot{M}_w for reasonable mass-accretion rates \dot{M}_a (or, equivalently, luminosities). Both quantities are uncertain at some level, but reasonable values are $\dot{M}_a \lesssim 10^{-8} \text{ M}_\odot \text{ yr}^{-1}$ ($L \lesssim 20L_\odot$ for a 0.7M_\odot white dwarf) and $\dot{M}_w \gtrsim 10^{-11} \text{ M}_\odot \text{ yr}^{-1}$ (where the upper limit is due to the uncertain correction for the ionization fractions of such species as C IV; a correction which could easily increase \dot{M}_w by a factor of 10). Significant progress has been made recently in models of radiation-driven disk winds (Pereyra, Kallman, & Blondin 1997; Proga, Stone, & Drew 1998; Feldmeir & Shlosman 1999), but none appear capable of satisfying these criteria. Pereyra, Kallman, & Blondin (1997) obtained $\dot{M}_w = 2 \times 10^{-14} \text{ M}_\odot \text{ yr}^{-1}$ for a $1L_\odot$ accretion disk; Proga, Stone, & Drew (1998) obtained $\dot{M}_w \leq 6 \times 10^{-12} \text{ M}_\odot \text{ yr}^{-1}$ for a $15L_\odot$ accretion disk; Feldmeir, Shlosman, & Vitello (1999) obtained $\dot{M}_w \sim 10^{-12} \text{ M}_\odot \text{ yr}^{-1}$ for a $10L_\odot$ accretion disk. Drew & Proga (2000) argued that the mass-accretion rates of high- \dot{M} CVs must be a higher than is presently understood for radiation pressure alone to drive the observed wind mass-loss rates.

Thanks to the edge-on geometry of OY Car, we can make a reasonably accurate estimate of the radiation force on the wind, which is simply the total luminosity of the lines divided by the speed of light: $\dot{P} = L/c$. The uncertainties are the conversion from flux to luminosity and the contribution from lines out of our bandpass, particularly lines between 200 \AA and the Lyman limit, which are hidden from us by interstellar absorption. Adding up the flux in the lines listed in Table 1, the observed *EUVE* spectrum provides a net radiation force of $\dot{P} \approx 4 \times 10^{20} \text{ dynes}$, but accounting for absorption by $\log N_H \text{ (cm}^{-2}\text{)} = 19.2\text{--}19.6$ increases this to $\dot{P} \approx 2\text{--}20 \times 10^{21} \text{ dynes}$. To determine the contribution from lines out of our bandpass we need a model of the intrinsic spectral energy distribution of the boundary layer and accretion disk and of the ionization state of the wind. To construct a fiducial model, we assume that the boundary layer radiates like a blackbody with $T_{\text{bl}} = 104 \text{ kK}$ and $f = 1$ (hence $L_{\text{bl}} = 5.0 \times 10^{34} \text{ erg s}^{-1} = 13L_\odot$) and that the disk has the standard Shakura-Sunyaev temperature profile and radiates locally like a blackbody with $L_{\text{disk}} = L_{\text{bl}}$ (hence $\dot{M}_a = 1.3 \times 10^{-8} \text{ M}_\odot \text{ yr}^{-1}$). If such a system were viewed face-on, it would have a flux density at 1500 \AA of $f_{1500} = 3.3 \times 10^{-11} (d/85 \text{ pc})^{-2} \text{ erg cm}^{-2} \text{ s}^{-1} \text{ \AA}^{-1}$ and a reasonable absolute visual magnitude of $M_V = 5.0$ (Warner 1987). The model spectrum extends from 1 to 7000 \AA (the entire range covered by the Verner, Verner, & Ferland 1996 line list), the wavelength bins are set at 3000 km s^{-1} , and all other wind parameters are as given in the previous section (in particular, $n = 10^{10} \text{ cm}^{-3}$ and $\dot{M}_w = 1.3 \times 10^{-10} \text{ M}_\odot \text{ yr}^{-1} = 0.01 \dot{M}_a$). We computed the wind’s ionization state exposed to the radiation fields of the boundary layer and accretion disk using the atomic physics packages in the current version of the Raymond & Smith (1977) spectral code. In particular, these codes use the Reilman & Manson (1979) photoionization cross sections and low-temperature dielectronic recombination rates from Nussbaumer & Storey (1983). For simplicity, the wind temperature is held fixed at 30 kK ; varying this quantity simply shifts the “horizontal” positions of the peaks of the various ionization fractions.

The results of our calculation are shown in Figure 11. The first panel shows the radiation force as a function of ionization parameter for the boundary layer alone (*dotted curve*) and the boundary layer plus accretion disk (*solid curve*). More detail is provided for the latter model in subsequent

panels. The second panel shows the contribution to the radiation force by the various elements: low- Z elements dominate the radiation force at low ionization parameters; O, Ne, and Ar dominate at intermediate ionization parameters; and Ne, Mg, and Fe dominate at high ionization parameters. The contribution by the various ions of O and Ne as well as the individual contributions of O VI $\lambda 150$, Ne V $\lambda 143$, and Ne VI $\lambda 123$ are shown in the third and fourth panels. That the model is properly normalized is indicated by the observed values of \dot{P} for these lines based on the fluxes in Table 1 and the assumption that $\log N_{\text{H}} \text{ (cm}^{-2}\text{)} = 19.4 \pm 0.2$. The ionization parameter of the wind is restricted to the range $\log \xi \approx 0\text{--}5$ by the weakness of O IV and Ne IV at the low end of the range and Ne VII and Fe IX at the high end of the range. To drive the wind to a terminal velocity of $V_{\infty} = 3000 \text{ km s}^{-1}$, we require $\dot{P} = \dot{M}_{\text{w}} V_{\infty} = 2.5 \times 10^{24} \text{ dynes}$, which is an order of magnitude larger than the model is capable of producing.

To investigate if other combinations of parameters produce more favorable results, we tested six other models along the trajectories of the model sequences from the previous section. With the assumption that $L_{\text{bl}} = 4\pi R_{\text{wd}}^2 f \sigma T_{\text{bl}}^4 = L_{\text{disk}} = GM_{\text{wd}} \dot{M}_{\text{a}} / 2R_{\text{wd}}$ and that the disk has the standard Shakura-Sunyaev temperature profile, the maximum disk temperature is $T_{\text{max}} = 0.49 (3f)^{1/4} T_{\text{bl}}$; requiring that $T_{\text{max}} \leq T_{\text{bl}}$ then limits the range of possible models to those with $f \leq 5.8$. Combined with the previous constraints, such models have EUV spectra which are dominated by the boundary layer and have net luminosities in the range $L = 2.6 \times 10^{34}\text{--}1.3 \times 10^{36} \text{ erg s}^{-1} = 6.8\text{--}340 L_{\odot}$. Wind densities (mass-loss rates) were taken from the results of the detailed model fits of the previous section. The resulting parameters for the six models (plus the above fiducial model) are listed in Table 3 and the results of the wind momentum calculations are shown in Figure 12. Only the models at the extreme ends of the two model sequences have $\dot{P} / \dot{M}_{\text{w}} V_{\infty}$ above unity, hence are capable of driving the required mass-loss rates. As shown in Table 3, however, these models are unrealistically bright in the UV ($f_{1500} \approx 1 \times 10^{-10} \text{ erg cm}^{-2} \text{ s}^{-1} \text{ \AA}^{-1}$) and optical ($M_V \approx 4$), and so are not likely realistic models of OY Car. Based on these results, we conclude that radiation pressure falls roughly an order of magnitude short of driving the wind of OY Car in superoutburst.

8. Discussion and Summary

Because of the longer time on source, the larger number of eclipses observed, and the higher count rate in the detector, the *EUVE* observations discussed here significantly strengthen previous reports that there is little or no eclipse by the secondary of the EUV emission region of OY Car in superoutburst. The mean *EUVE* spectrum extends from 70 to 190 \AA and contains broad (FWHM $\approx 1 \text{ \AA}$) emission lines of N V, O V–O VI, Ne V–Ne VII, Mg IV–Mg VI, Fe VI–Fe VIII, and possibly Fe XXIII. The gross details of the spectrum are reproduced by the spectrum of a collisionally ionized plasma with a temperature $T \approx 320 \text{ kK}$, an absorbing column density $N_{\text{H}} \approx 3.4 \times 10^{19} \text{ cm}^{-2}$, and an emission measure $EM \approx 3.2 \times 10^{55} \text{ cm}^{-3}$, but such a model fails to reproduce the observed spectrum in detail. Better fits are obtained with a model (similar to that of Seyfert 2 galaxies) wherein radiation from the boundary layer and accretion disk is scattered into the line of sight by

the system’s cool ($T \sim 30$ kK) photoionized accretion disk wind. The likely range of acceptable parameters for the boundary layer are $T_{\text{bl}} \approx 90\text{--}130$ kK and $N_{\text{H}} \approx 1.6\text{--}3.5 \times 10^{19} \text{ cm}^{-2}$. This range for the absorbing column density is typical of the interstellar column densities of nearby CVs beyond the Local Bubble (Mauche, Raymond, & Córdova 1988; Polidan, Mauche, & Wade 1990; Long et al. 1996), while the range of boundary layer temperatures is significantly less than that of SS Cyg ($T_{\text{bl}} \approx 230\text{--}350$ kK; Mauche, Raymond, & Mattei 1995) but comparable to that of U Gem ($T_{\text{bl}} = 110\text{--}140$ kK; Long et al. 1996) and VW Hyi ($T_{\text{bl}} \approx 120$ kK; Mauche 1996). The corresponding range of the boundary layer luminosity is less clear because it is possible to trade off the intensity of the EUV continuum for the wind optical depth (i.e., the wind mass-loss rate). A lower limit to the fractional emitting area of the boundary layer is $f \approx 0.1$, and a lower limit to the boundary layer luminosity is $L_{\text{bl}} \approx 1 \times 10^{34} \text{ erg s}^{-1} \approx 3 L_{\odot}$. Adding a “minimal” Shakura-Sunyaev accretion disk¹ with $L_{\text{disk}} = GM_{\text{wd}}\dot{M}_{\text{a}}/2R_{\text{wd}} = L_{\text{bl}} = 4\pi R_{\text{wd}}^2 f \sigma T_{\text{bl}}^4$ provides further constraints. Requiring that the maximum disk temperature be less than or equal to the boundary layer temperature requires that $f \leq 5.8$ and $L_{\text{bl}} \leq 6.5 \times 10^{35} \text{ erg s}^{-1} \approx 170 L_{\odot}$. Adding reasonable brightness constraints in the UV [$f_{1500} \lesssim 1 \times 10^{-10} (d/85 \text{ pc})^{-2} \text{ erg cm}^{-2} \text{ s}^{-1} \text{ \AA}^{-1}$] and optical ($M_V \gtrsim 5$) is equivalent to the requirement that the mass-accretion rate $\dot{M}_{\text{a}} \lesssim 10^{-8} M_{\odot} \text{ yr}^{-1}$, consistent with observations of other high- \dot{M} CVs, hence $L_{\text{bl}} \lesssim 4 \times 10^{34} \text{ erg s}^{-1} \approx 10 L_{\odot}$. Such models have wind mass-loss rates of $\dot{M}_{\text{w}} \lesssim 10^{-10} M_{\odot} \text{ yr}^{-1} \approx 0.01 \dot{M}_{\text{a}}$ and fall an order of magnitude short of driving the wind by radiation pressure alone. An alternative is that the wind of OY Car is driven by a combination of radiation pressure and magnetic forces (a magnetocentrifugal wind). Such winds have been investigated recently by Proga (2000).

The observations described here could not have been accomplished without the alert provided by M. Mattiazzo and the optical data provided by M. Mattiazzo, N. Suntzeff, M. Keane, P. Nelson, R. Stubbings, T. Cragg, and J. Herr. Rapid response to the outburst was facilitated by J. Mattei, Director of the AAVSO; F. Bateson, Director of the VSS/RASNZ; and VSNET. Members of the AAVSO and RASNZ provided the visual magnitude estimates from which the optical light curve was assembled. Special thanks go to W. Walker for the optical photometry shown in Figure 3. The *EUVE* target-of-opportunity observations were made possible by the rapid response of *EUVE* Acting Deputy Director J. Vallergera, *EUVE* Science Planner B. Roberts, the staff of the *EUVE* Science Operations Center at CEA, and the Flight Operations Team at Goddard Space Flight Center. K. Dere kindly provided assistance with CHIANTI. The manuscript was improved by the comments and suggestions of the referee, K. Long. C. W. M.’s contribution to this work was performed under the auspices of the U.S. Department of Energy by University of California Lawrence Livermore National Laboratory under contract No. W-7405-Eng-48.

¹The observed values of $L_{\text{disk}}/L_{\text{bl}}$ range from ≈ 2 for U Gem (Long et al. 1996), $\gtrsim 10$ for SS Cyg (Mauche, Raymond, & Mattei 1995), and ~ 20 for VW Hyi (Mauche 1996).

Table 1. Line Parameters and Identifications

Line Parameters		Line Identifications			
Wavelength (Å)	Flux (10^{-13} erg cm $^{-2}$ s $^{-1}$)	Wavelength (Å)	Ion	Transition	Oscillator Strength
95.59 \pm 0.08	1.0 \pm 0.2	95.446	Mg VI	$2p^3-2p^23d$	1.26E+00
97.64 \pm 0.08	1.2 \pm 0.2	97.495	Ne VII	$2s^2-2s3p$	4.86E-01
		98.215	Ne VI	$2p-4d$	1.22E-01
		98.477	Fe VIII	$3d-6f$	1.05E-01
100.09 \pm 0.13	0.7 \pm 0.2	99.688	O VI	$2s-6p$	1.69E-02
101.61 \pm 0.11	0.8 \pm 0.2	101.309	Ne VI	$2s^22p-2s2p3p$	2.78E-02
		101.501	Ne VI	$2s^22p-2s2p3p$	1.97E-02
105.08 \pm 0.09	1.0 \pm 0.2	103.999	Mg V	$2p^4-2p^34s$	1.56E-01
		104.035	Mg V	$2p^4-2p^34d$	1.56E-01
		104.813	O VI	$2s-5p$	3.20E-02
108.05 \pm 0.07	1.4 \pm 0.2	107.993	Fe VIII	$3d-5f$	1.97E-01
109.66 \pm 0.07	1.4 \pm 0.2	109.411	Ne VI	$2s^22p-2s2p3p$	2.92E-02
111.41 \pm 0.05	2.6 \pm 0.2	110.924	Mg V	$2p^4-2p^33d$	1.91E-01
		111.147	Ne VI	$2s^22p-2s2p3p$	1.68E-01
		111.668	Mg VI	$2p^3-2p^23s$	1.24E-01
		111.675	Fe VII	$3d^2-3d7f$	8.09E-02
112.81 \pm 0.08	1.3 \pm 0.2	112.479	Fe VIII	$3p^63d-3p^53d4s$	9.30E-02
		113.293	Fe VIII	$3p^63d-3p^53d4s$	5.45E-02
114.53 \pm 0.03	4.2 \pm 0.2	113.812	Mg V	$2p^4-2p^33d$	9.69E-02
		114.135	Mg V	$2p^4-2p^33d$	2.87E-01
		114.200	Ne VI	$2s^22p-2s2p3p$	1.04E-01
		114.358	O V	$2s^2-2s8p$	1.02E-02
		114.887	Mg V	$2p^4-2p^33d$	2.43E-01
116.20 \pm 0.06	2.2 \pm 0.2	115.824	O VI	$2s-4p$	7.41E-02
		116.161	O V	$2s^2-2s7p$	1.39E-02
		116.773	Fe VIII	$3p^63d-3p^53d4s$	1.11E-01
117.60 \pm 0.06	2.4 \pm 0.2	117.269	Fe VII	$3d^2-3d6f$	5.31E-02
		118.000	O V	$2s^2-2p4d$	5.68E-03
119.28 \pm 0.04	3.9 \pm 0.3	118.911	Ne V	$2p^2-2p4d$	1.78E-01
		119.047	Fe VIII	$3p^63d-3p^53d4s$	4.25E-02
		119.102	O V	$2s^2-2s6p$	2.95E-02
120.56 \pm 0.24	0.7 \pm 0.3	120.250	Fe VII	$3d^2-3d6f$	1.34E-01
121.59 \pm 0.15	1.7 \pm 0.3	121.781	Mg V	$2p^4-2p^33d$	2.59E-01
122.87 \pm 0.03	9.4 \pm 0.4	122.619	Ne VI	$2p-3d$	5.71E-01
		123.340	Mg IV	$2p^5-2p^45d$	9.07E-02

Table 1—Continued

Line Parameters		Line Identifications			
Wavelength (Å)	Flux (10^{-13} erg cm $^{-2}$ s $^{-1}$)	Wavelength (Å)	Ion	Transition	Oscillator Strength
124.56 \pm 0.11	1.7 \pm 0.3	124.616	O V	$2s^2-2s5p$	5.00E–02
125.67 \pm 0.06	3.4 \pm 0.3	125.245	Na V	$2p^3-2p^23d$	1.11E+00
127.49 \pm 0.08	3.0 \pm 0.4	127.179	Fe VII	$3p^63d^2-3p^53d^24s$	1.18E–01
128.40 \pm 0.15	1.8 \pm 0.4	128.581	Fe VII	$3d^2-3d5f$	1.21E–01
129.98 \pm 0.10	2.2 \pm 0.3	129.729	Al IV	$2p^6-2p^53d$	7.78E–01
		129.925	Mg IV	$2p^5-2p^44d$	5.09E–02
		130.027	Mg IV	$2p^5-2p^44d$	1.65E–01
		130.374	Fe VII	$3d^2-3d5f$	2.63E–01
131.33 \pm 0.04	7.8 \pm 0.4	131.121	Fe VIII	$3d-4f$	5.68E–01
132.65 \pm 0.06	4.6 \pm 0.4	132.007	Ne V	$2s^22p^2-2s2p^23p$	1.05E–01
		132.830	Fe XXIII	$2s^2-2s2p$	1.52E–01
		132.941	Mg IV	$2p^5-2p^43d$	4.50E–02
134.17 \pm 0.15	1.2 \pm 0.3
136.07 \pm 0.05	4.0 \pm 0.3	135.523	O V	$2s^2-2s4p$	7.77E–02
137.68 \pm 0.14	2.3 \pm 0.5
138.65 \pm 0.08	4.2 \pm 0.5	138.555	Ne VI	$2p-3s$	2.83E–02
		139.029	O V	$2s^2-2p3d$	5.79E–02
140.77 \pm 0.13	1.8 \pm 0.3	140.296	Mg IV	$2p^5-2p^43d$	1.42E–01
		140.357	N V	$2s-6p$	1.59E–02
		140.571	Mg IV	$2p^5-2p^43d$	7.90E–02
		140.652	Mg IV	$2p^5-2p^43d$	1.65E–01
142.44 \pm 0.19	1.9 \pm 0.5	142.615	Ne V	$2p^2-2p3d$	2.27E–01
143.51 \pm 0.05	8.8 \pm 0.6	143.316	Ne V	$2p^2-2p3d$	6.73E–01
145.51 \pm 0.18	1.5 \pm 0.3
147.14 \pm 0.11	2.8 \pm 0.4	146.790	Mg IV	$2p^5-2p^43d$	8.47E–02
		147.153	Mg IV	$2p^5-2p^43d$	3.28E–01
		147.425	N V	$2s-5p$	3.00E–02
148.85 \pm 0.17	2.0 \pm 0.4	148.843	Ne IV	$2p^3-2p^24d$	2.89E–01
150.33 \pm 0.08	6.1 \pm 0.6	150.101	O VI	$2s-3p$	2.65E–01
		150.922	Fe VII	$3d^2-3d4f$	6.58E–01
151.69 \pm 0.11	4.0 \pm 0.5	151.682	Fe VII	$3d^2-3d4f$	4.61E–01
153.37 \pm 0.95	0.4 \pm 0.4
154.96 \pm 0.19	2.7 \pm 0.6
156.06 \pm 0.36	1.2 \pm 0.6
158.44 \pm 0.28	1.1 \pm 0.4	157.717	Ne IV	$2p^3-2p^24s$	4.55E–02

Table 1—Continued

Line Parameters		Line Identifications			
Wavelength (Å)	Flux (10^{-13} erg cm $^{-2}$ s $^{-1}$)	Wavelength (Å)	Ion	Transition	Oscillator Strength
160.59 ± 0.33	1.1 ± 0.5
162.65 ± 0.35	1.1 ± 0.5	162.559	N V	$2s-4p$	6.86E-02
165.61 ± 0.12	3.7 ± 0.6	165.530	Fe VI	$3p^6 3d^3-3p^5 3d^4$	4.97E-01
168.53 ± 0.06	8.6 ± 0.7	168.638	Fe VIII	$3p^6 3d-3p^5 3d^2$	5.70E-01
171.54 ± 0.14	4.0 ± 0.7	171.073	Fe IX	$3p^6-3p^5 3d$	3.05E+00
		171.873	Mg IV	$2p^5-2p^4 3s$	7.12E-02
		172.169	O V	$2s^2-2s 3p$	3.95E-01
		172.567	Ne IV	$2p^3-2p^2 3d$	9.27E-01

Table 2. Scattering Model Parameters

Parameter	Model 1-7b	Model 1-5b	Model 2-5b	Model 2-3b
T_{bl} (kK)	107	120	98.6	102
N_{H} (cm $^{-2}$)	2.1×10^{19}	1.8×10^{19}	3.2×10^{19}	3.1×10^{19}
f	0.27	0.17	3.4	6.5
L_{bl} (erg s $^{-1}$) ..	1.5×10^{34}	1.5×10^{34}	1.4×10^{35}	3.1×10^{35}
$\chi'(\text{N})$	1.0	0.3	0.3	0.1
$\chi'(\text{O V})$	0.5	0.2	0.19	0.06
$\chi'(\text{O VI})$	0.2	0.08	0.09	0.03
$\chi'(\text{Ne V})$	1.0	0.32	0.37	0.11
$\chi'(\text{Ne VI})$	2.5	0.72	0.68	0.19
$\chi'(\text{Ne VII})$	0.5	0.1	0.1	0.02
$\chi'(\text{Na})$	1.0	0.3	0.3	0.1
$\chi'(\text{Mg})$	1.0	0.3	0.3	0.1
$\chi'(\text{Al})$	1.0	0.3	0.3	0.1
$\chi'(\text{Ar})$	1.0	0.3	0.3	0.1
$\chi'(\text{Fe VI})$	1.0	0.3	0.6	0.2
$\chi'(\text{Fe VII})$	0.6	0.4	0.3	0.1
$\chi'(\text{Fe VIII})$	3.0	1.0	1.0	0.3
$\chi'(\text{Fe XXIII})$. . .	4.0	1.5	1.5	0.5

REFERENCES

- Abbott, M. J., et al. 1996, *ApJS*, 107, 451
- Allen, C. W. 1973, *Astrophysical Quantities* (London: Athlone Press)
- Arnaud, M., & Raymond, J. 1985, *ApJ*, 398, 394
- Arnaud, M., & Rothenflug, R. 1985, *A&AS*, 60, 425
- Blandford, R. D., & Payne, D. G. 1982, *MNRAS*, 199, 883
- Bowyer, S., & Malina, R. F. 1991, in *Extreme Ultraviolet Astronomy*, ed. R. F. Malina & S. Bowyer (New York: Pergamon), 397
- Bruch, A., Beele, D., & Baptista, R. 1996, *A&A*, 306, 151
- Cannizzo, J. 1993, in *Accretion Disks in Compact Stellar Systems*, ed. J. C. Wheeler (Singapore: World Sci. Pub.), 6
- Cannizzo, J. K., & Pudritz, R. E. 1988, *ApJ*, 327, 840
- Craig, N., et al. 1997, *ApJS*, 113, 131
- Done, C., & Osborne, J. P. 1997, *MNRAS*, 288, 649
- Drew, J. E., & Proga, D. 2000, in *Proceedings of the Brian Warner Symposium*, in press
- Feldmeir, A., & Shlosman, I. 1999, *ApJ*, 526, 344
- Feldmeir, A., Shlosman, I., & Vitello, P. 1999, *ApJ*, 526, 357
- Heap, S. R., et al. 1978, *Nature*, 275, 385
- Kelly, R. L. 1987, *Atomic and Ionic Spectrum Lines below 200 Angstroms: Hydrogen through Krypton* (New York: AIP)
- Klare, J., et al. 1982, *A&A*, 102, 337
- Krautter, J., et al. 1981, *A&A*, 102, 337
- Landi, E., Landini, M., Dere, K. P., Young, P. R., & Mason, H. E. 1999, *A&AS*, 135, 339
- Long, K. S., Mauche, C. W., Raymond, J. C., Szkody, P., & Mattei, J. A. 1996, *ApJ*, 469, 841
- Lubow, S. H. 1991, *ApJ*, 381, 259
- Mason, K. O., Córdova, F. A., Watson, M. G., & King, A. R. 1988, *MNRAS*, 232, 779

- Mauche, C. W. 1996, in *Cataclysmic Variables and Related Objects*, ed. A. Evans & J. H. Wood (Dordrecht: Kluwer), 243
- Mauche, C. W. 1997, in *X-ray Imaging and Spectroscopy of Cosmic Hot Plasmas*, ed. F. Makino & K. Mitsuda (Tokyo: Univ. Academy Press), 529
- Mauche, C. W., Raymond, J. C., & Córdova, F. A. 1988, *ApJ*, 335, 829
- Mauche, C. W., Raymond, J. C., & Mattei, J. A. 1995, *ApJ*, 446, 842
- Mazzotta, P., Mazzitelli, G., Colafrancesco, S., & Vittorio, N. 1998, *A&AS*, 133, 403
- Mewe, R., Gronenschild, E. H. B. M., & van den Oord, G. H. J. 1985, *A&AS*, 62, 197
- Mukai, K., Wood, J. H., Naylor, T., Schlegel, E. M., & Swank, J. H. 1997, *ApJ*, 475, 812
- Murray, J. R. 1998, *MNRAS*, 297, 323
- Narayan, R., & Popham, R. 1993, *Nature*, 362, 820
- Naylor, T., et al. 1988, *MNRAS*, 231, 237
- Nussbaumer, H., & Storey, P. J. 1983, *A&A*, 126, 75
- Osaki, Y. 1996, *PASP*, 108, 39
- Pereyra, N. A., Kallman, T. R., & Blondin, J. M. 1997, *ApJ*, 477, 368
- Polidan, R. S., & Holberg, J. B. 1987, *MNRAS*, 225, 131
- Polidan, R. S., Mauche, C. W., & Wade, R. A. 1990, *ApJ*, 356, 211
- Popham, R., & Narayan, R. 1995, *ApJ*, 442, 337
- Pratt, G. W., Hassall, B. J. M., Naylor, T., & Wood, J. H. 1999a, *MNRAS*, 307, 413
- Pratt, G. W., Hassall, B. J. M., Naylor, T., Wood, J. H., & Patterson, J. 1999b, *MNRAS*, 309, 847
- Pringle, J. E. 1977, *MNRAS*, 178, 195
- Pringle, J. E., et al. 1987, *MNRAS*, 225, 73
- Pringle, J. E., & Savonije, G. J. 1979, *MNRAS*, 187, 777
- Proga, D. 2000, *ApJ*, submitted
- Proga, D., Stone, J. M., & Drew, J. E. 1998, *MNRAS*, 295, 595
- Raymond, J. C., & Smith, B. W. 1977, *ApJS*, 35, 419

- Reilman, R. F., & Manson, S. T. 1979, *ApJS*, 40, 815
- Sirk, M. M., Vallergera, J. V., Finley, D. S., Jelinsky, P., & Malina, R. F. 1997, *ApJS*, 110, 347
- Szkody, P., Long, K. S., Sion, E. M., & Raymond, J. C. 1996, *ApJ*, 469, 834
- Tylenda, R. 1977, *Acta Astr.*, 27, 235
- Tylenda, R. 1981, *Acta Astr.*, 31, 267
- van Teeseling, A. 1997, *A&A*, 319, L25
- van Teeseling, A., Beuermann, K., & Verbunt, F. 1996, *A&A*, 315, 467
- Verner, D. A., Verner, E. M., & Ferland, G. J. 1996, *Atomic Data and Nuc. Data Tables*, 64, 1
- Warner, B. 1995, *Cataclysmic Variable Stars* (Cambridge: CUP)
- Warner, B. 1987, *MNRAS*, 227, 23
- Wood, J. H., Horne, K., Berriman, G., & Wade, R. A. 1989, *ApJ*, 341, 974
- Wood, J. H., Naylor, T., Hassall, B. J. M., & Ramseyer, T. F. 1995, *MNRAS*, 273, 772
- Wood, J. H., Naylor, T., & Marsh, T. R. 1995, *MNRAS*, 274, 31

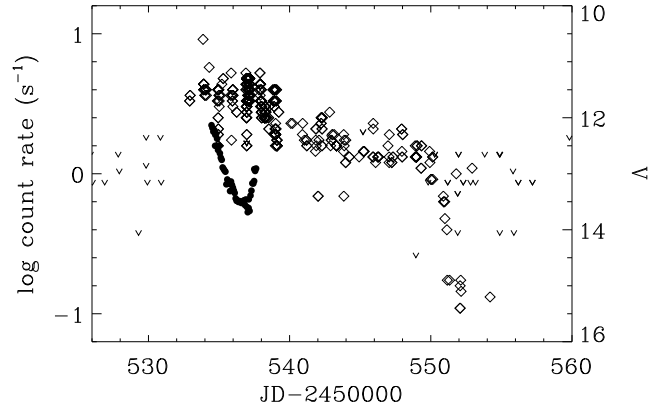


Fig. 1.— DS count rate and AAVSO and RASNZ optical light curves. DS measurements are shown by the filled circles; optical measurements and upper limits are shown by the diamonds and carets, respectively. Optical eclipses are excluded from this presentation by restricting the binary phases to $0.1 \leq \phi \leq 0.9$.

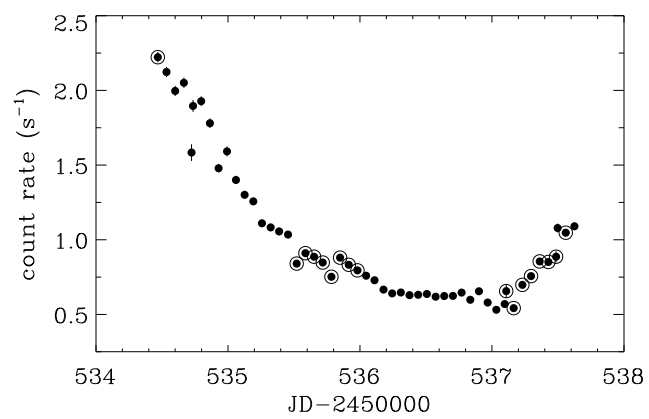


Fig. 2.— DS count rate light curve. Orbits containing eclipses of the white dwarf are marked with circles. Error bars are typically smaller than the symbols.

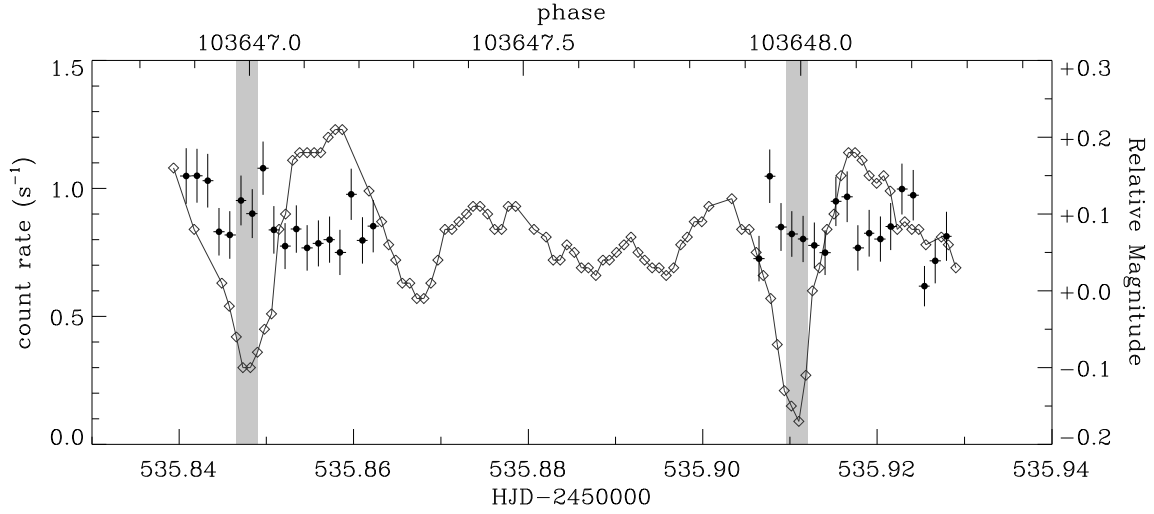


Fig. 3.— DS count rate and optical light curves for the interval $\text{HJD} - 2450000 = 535.84\text{--}535.93$. DS measurements are shown by the filled circles with error bars, relative optical measurements are shown by the diamonds connected by straight lines. Binary phase is relative to the ephemeris of Pratt et al. (1999a). The grey stripes denote the phase intervals when the white dwarf is eclipsed by the secondary ($-0.02 \leq \phi \leq +0.02$).

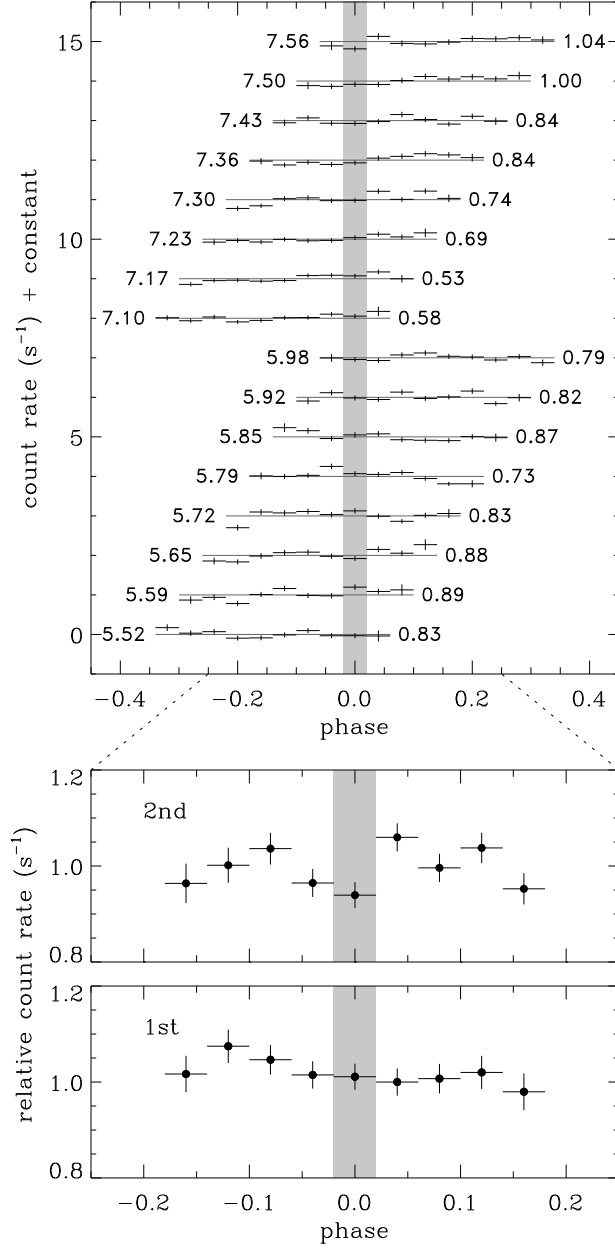


Fig. 4.— *Upper panel*: DS count rate light curves from individual *EUVE* orbits. Label to the right of each curve is the date (HJD - 2450530) of the midpoint of the orbit, while that to the right is the weighted mean count rate \bar{c} . Each successive orbit of data is offset vertically by $n - \bar{c}$, where $n = 0, 1, \dots, 15$. *Lower panels*: Mean relative DS light curves from the first and second groups of eclipse intervals shown in the upper panel. The grey stripes denote the phase interval when the white dwarf is eclipsed by the secondary ($-0.02 \leq \phi \leq +0.02$).

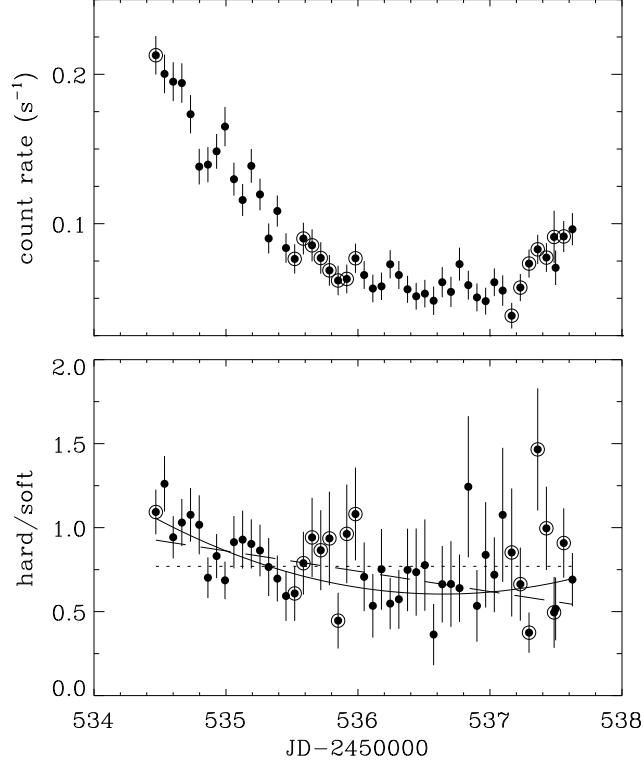


Fig. 5.— SW count rate (*upper panel*) and hardness ratio (*lower panel*) light curves. Hardness ratio is defined as the ratio of the background-subtracted SW counts from 90–125 Å to that from 125–180 Å. Constant, linear, and quadratic fits of the hardness ratio are indicated respectively by the dotted, dashed, and solid curves.

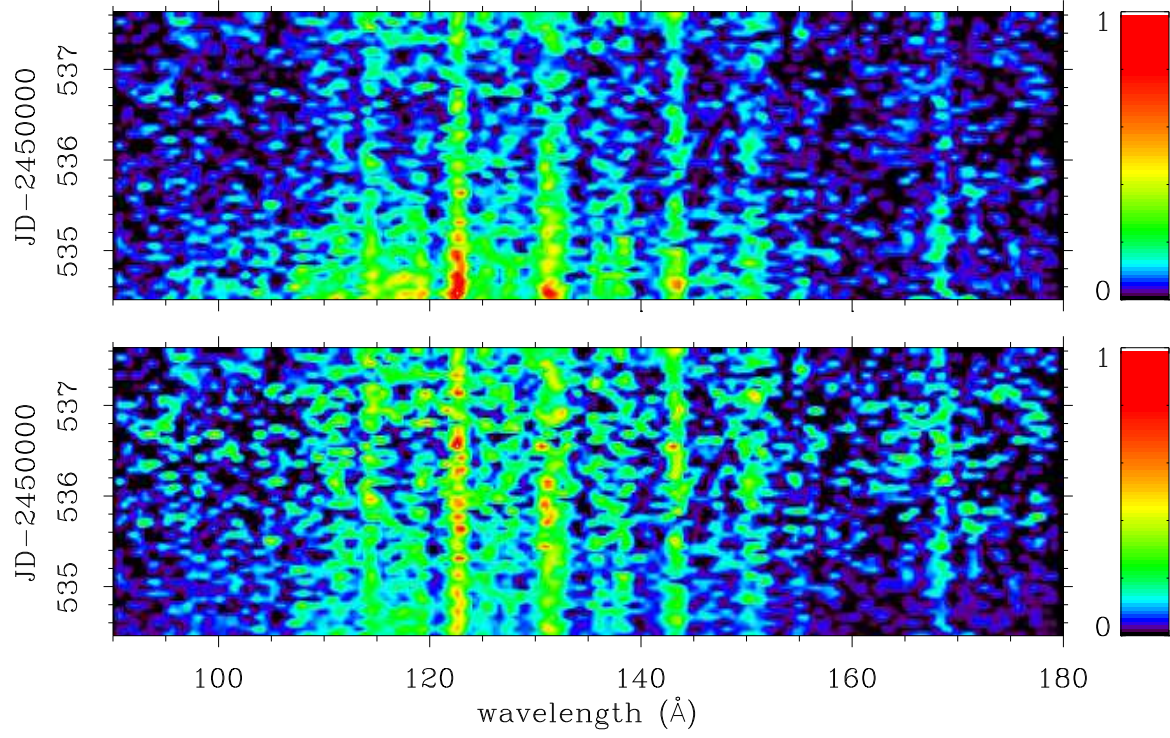


Fig. 6.— Pseudotrained SW spectrum. *Upper panel:* spectra as observed. *Lower panel:* spectra normalized to an equal number of counts between 90 and 180 Å.

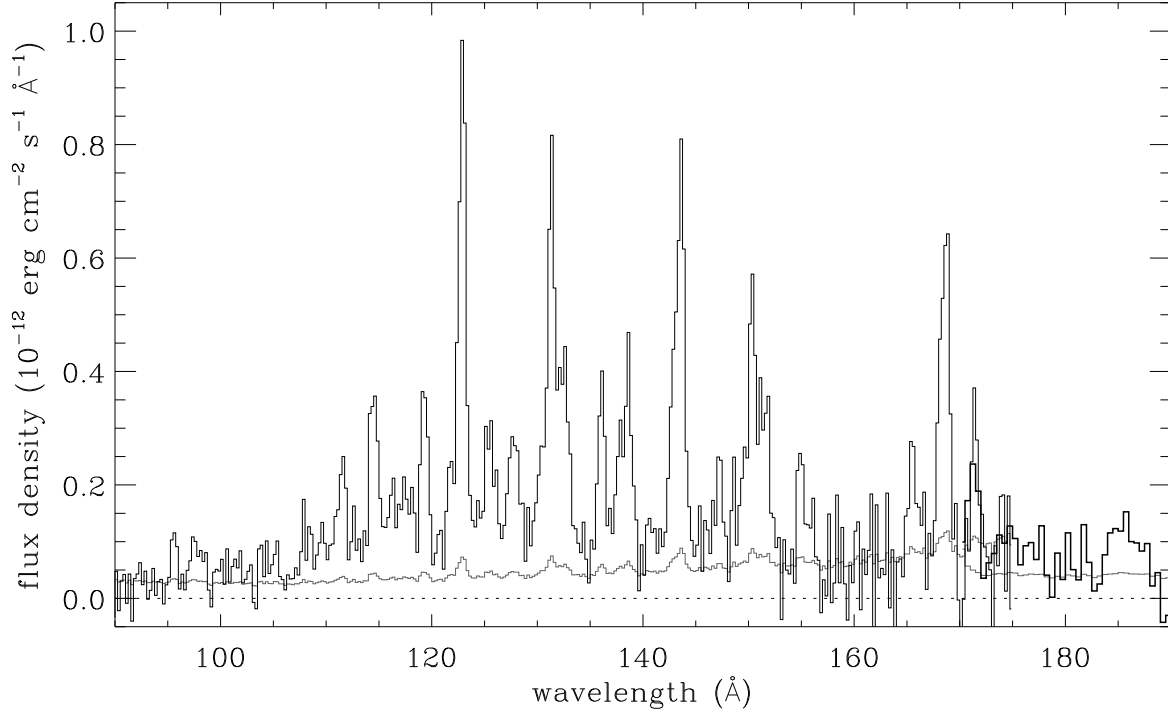


Fig. 7.— Mean SW and MW spectra. The SW spectrum ends at 175 Å while the MW spectrum begins at 170 Å. Traces at the bottom of the figure are the associated 1σ error vectors.

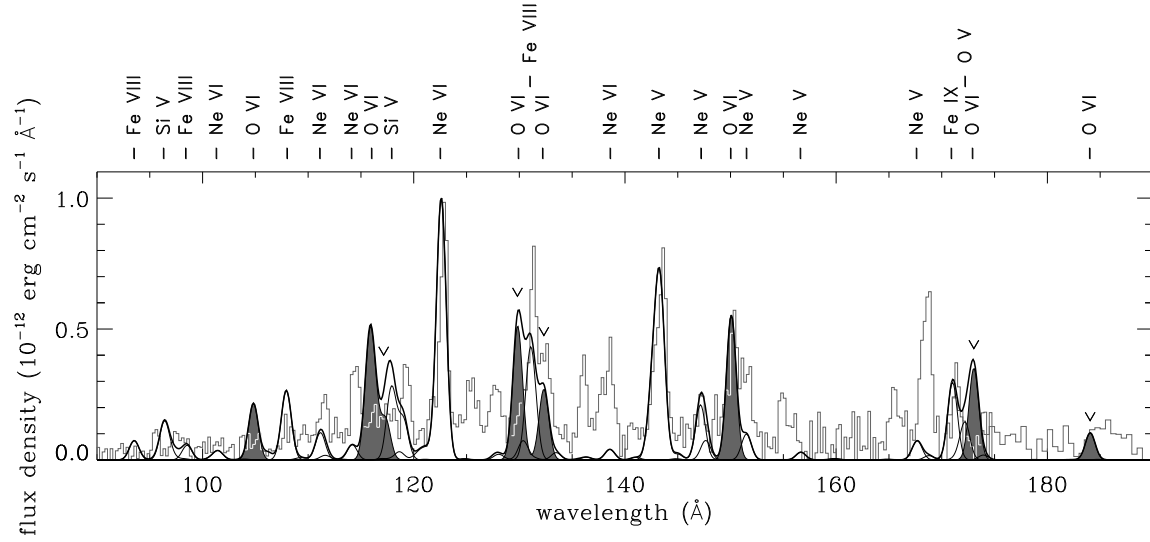


Fig. 8.— CHIANTI collisional plasma model of the mean *EUVE* spectrum of OY Car with $\log T(\text{K}) = 5.5$, $N_{\text{H}} = 3.4 \times 10^{19} \text{ cm}^{-2}$, $EM = 3.2 \times 10^{55} \text{ cm}^{-3}$, and convolved with a $\text{FWHM} = 1.08 \text{ \AA}$ Gaussian. The observed spectrum is shown by the grey histogram, the net model spectrum by the thick solid curve, and the spectra of the various ions by the thin solid curves. The O VI model spectrum is shaded and its nonresonance lines are indicated by carets.

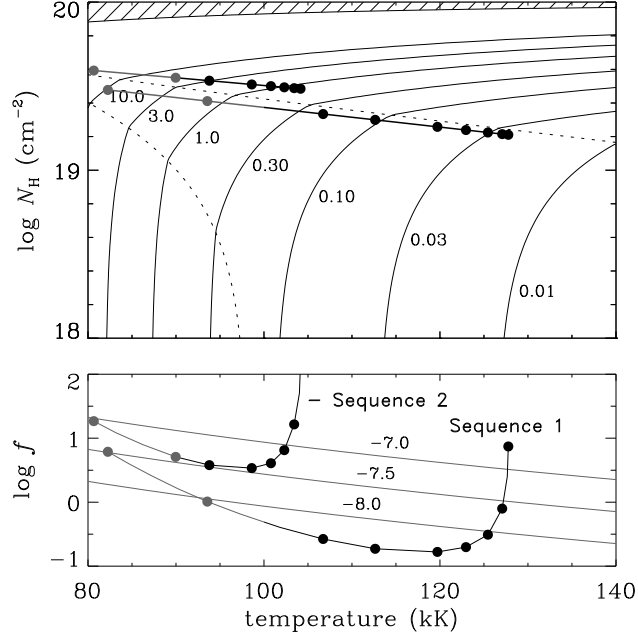


Fig. 9.— *Upper panel:* Fractional emitting area f for $\tau = \infty$ as a function of temperature T_{bl} and absorbing column density N_{H} . Favorable continuum models lie near the upper dotted curve. Models in the hatched region exceed the Eddington limit. Solid lines are the locus of points satisfying the Fe VIII emission line flux constraints. *Lower panel:* Fractional emitting area f satisfying the Fe VIII emission line flux constraints with $\chi'(\text{Fe VIII}) = [0.01, 0.1, 0.3, 0.6, 1, 2, 3, 6, 10]$. Grey curves are contours of constant luminosity $L_{\text{bl}} = 4\pi R_{\text{wd}}^2 f \sigma T_{\text{bl}}^4 = GM_{\text{wd}} \dot{M}_{\text{a}} / 2R_{\text{wd}}$ for $\dot{M}_{\text{a}} = 10^{-8}$, $10^{-7.5}$, and $10^{-7} \text{ M}_{\odot} \text{ yr}^{-1}$.

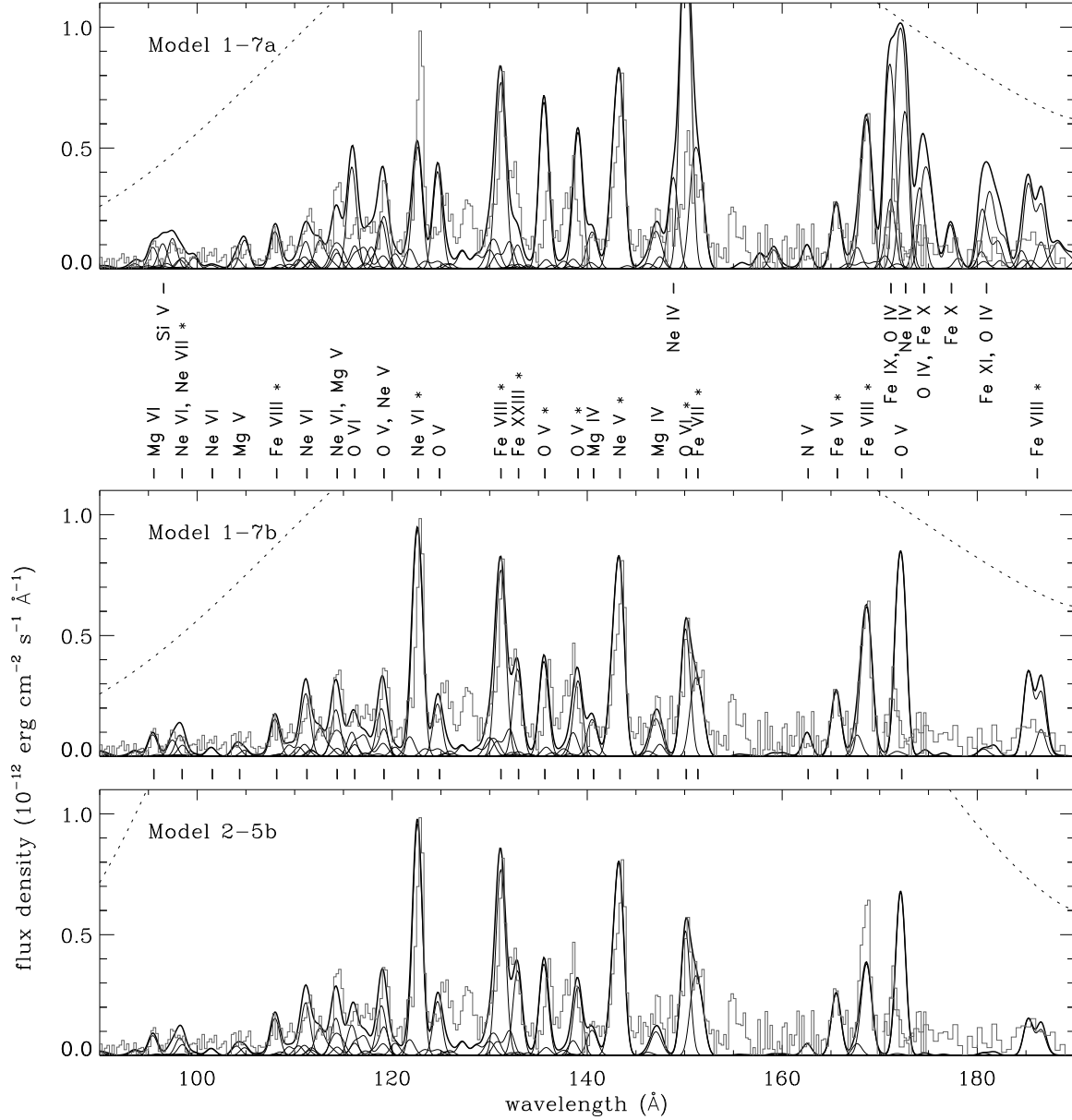


Fig. 10.— Representative scattering models of the mean *EUVE* spectrum of OY Car. The observed spectrum is shown by the grey histogram, the absorbed blackbody continua by the dotted curves, the net model spectra by the thick solid curves, and the spectra of the various ions by the thin solid curves. The lines marked with asterisks were adjusted to achieve the fits shown. Refer to Table 2 for model parameters.

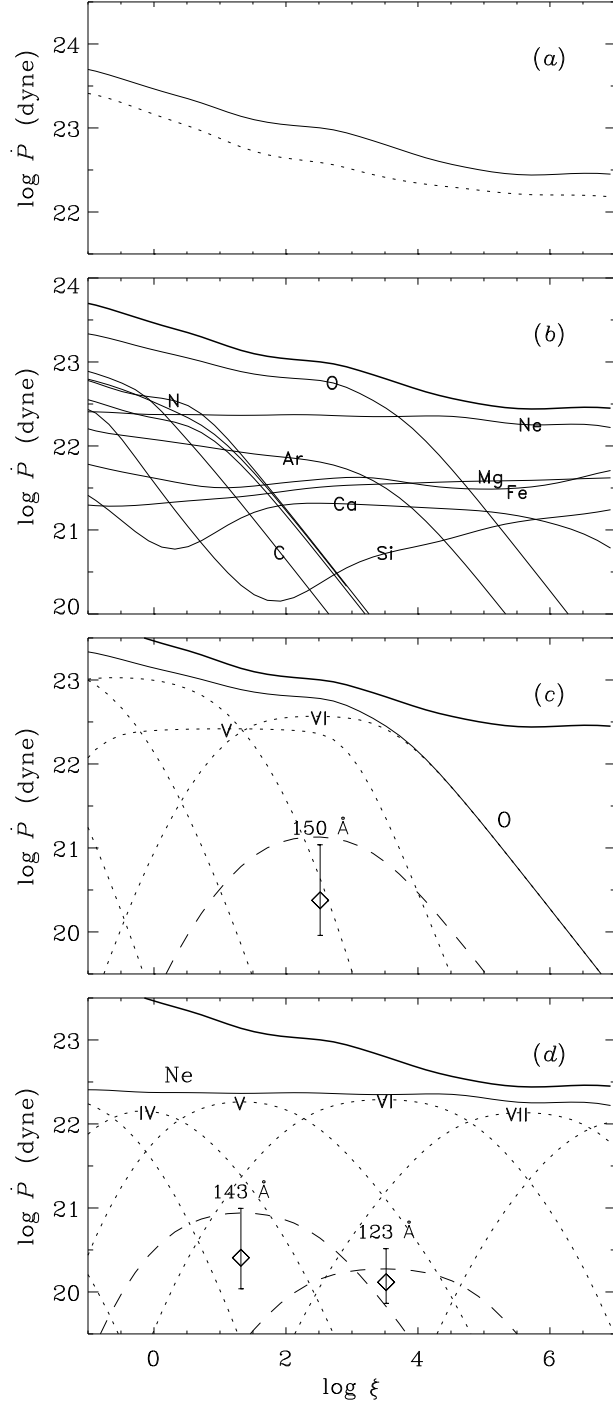


Fig. 11.— Radiation force $\dot{P} = L/c$ as a function of ionization parameter ξ . (a) Total force from the boundary layer alone with $T_{\text{bl}} = 104$ kK and $f = 1$ (hence $L_{\text{bl}} = 13 L_{\odot}$) (*dotted curve*) and the boundary layer plus accretion disk with $L_{\text{disk}} = L_{\text{bl}}$ (*solid curve*). (b) Contributions from the various elements, (c) ions of O, and (d) ions of Ne for the model with $L_{\text{disk}} = L_{\text{bl}}$. Curves labeled “150 Å”, “143 Å”, and “123 Å” are respectively the contributions of O VI $\lambda 150$, Ne V $\lambda 143$, and Ne VI $\lambda 123$. Data points are the observed values of these lines assuming $d = 85$ pc and $\log N_{\text{H}} (\text{cm}^{-2}) = 19.4 \pm 0.2$.

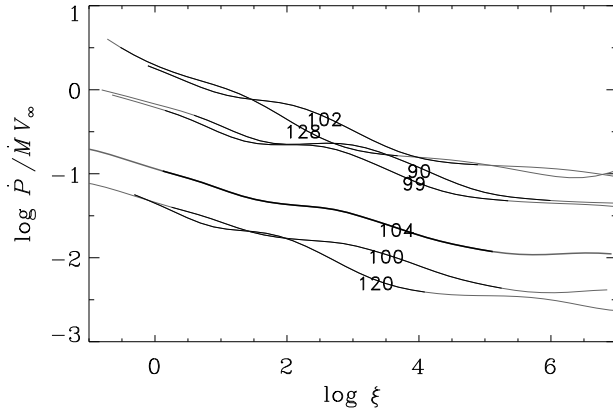


Fig. 12.— Radiation force \dot{P} relative to the wind momentum $\dot{M}_w V_\infty$ as a function of ionization parameter ξ . Various curves are labeled with the boundary layer temperature T_{bl} (kK) and are dark where the models likely apply: where the contributions of O VI $\lambda 150$, Ne V $\lambda 143$, or Ne VI $\lambda 123$ are within a half a magnitude of their peak values.

Table 3. Radiation Force Model Parameters

T_{bl} (kK)	N_{H} (cm^{-2})	f	L_{bl} (erg s^{-1})	\dot{M}_{a} ($\text{M}_{\odot} \text{ yr}^{-1}$)	f_{1500} ($\text{erg cm}^{-2} \text{ s}^{-1} \text{ \AA}^{-1}$)	V (mag)	M_V (mag)	\dot{M}_{w} ($\text{M}_{\odot} \text{ yr}^{-1}$)	\dot{P} (dyne)
104	2.5×10^{19}	1.0	5.0×10^{34}	1.3×10^{-8}	3.3×10^{-11}	9.7	5.0	1.3×10^{-10}	2.5×10^{24}
100	2.4×10^{19}	0.49	2.1×10^{34}	5.7×10^{-9}	1.6×10^{-11}	10.2	5.5	1.3×10^{-10}	2.5×10^{24}
120	1.8×10^{19}	0.17	1.5×10^{34}	4.0×10^{-9}	1.1×10^{-11}	10.4	5.8	4.0×10^{-11}	7.6×10^{23}
128	1.6×10^{19}	3.0	3.5×10^{35}	9.2×10^{-8}	1.4×10^{-10}	8.7	4.0	1.3×10^{-12}	2.5×10^{22}
90.0	3.6×10^{19}	5.1	1.4×10^{35}	3.9×10^{-8}	8.0×10^{-11}	9.1	4.4	4.0×10^{-11}	7.6×10^{23}
98.6	3.2×10^{19}	3.4	1.4×10^{35}	3.7×10^{-8}	7.6×10^{-11}	9.1	4.5	4.0×10^{-11}	7.6×10^{23}
102	3.1×10^{19}	6.5	3.1×10^{35}	8.2×10^{-8}	1.4×10^{-10}	8.7	4.1	1.3×10^{-11}	2.5×10^{23}